coatings

MDPI

Article

Biomass-Derived Hard Carbon Materials for High-Performance Sodium-Ion Battery

Yixing Chen, Jiaming Cui, Sheng Wang *, Wentao Xu and Ruoqi Guo

State Key Laboratory of Advanced Processing and Recycling of Non-Ferrous Metals, Lanzhou University of Technology, Lanzhou 730050, China; cyx18829789528@163.com (Y.C.); 18329695126@163.com (J.C.); 18145154763@163.com (W.X.); guoruoqi477477@163.com (R.G.)
* Correspondence: wangtion@163.com

Abstract: Using biomass-derived hard carbon materials as anode materials for sodium-ion batteries has facilitated resource recycling and brought significant economic benefits. However, the main obstacles to the large-scale application of these materials are the low Coulombic efficiency and high irreversible capacity of hard carbon materials. This study used waste moso bamboo as a carbon source to prepare and pre-oxidize hard carbon through a stepped temperature sintering process. The introduction of oxygen atoms into the carbon layers has been shown to increase the spacing between the carbon layers, which facilitates the insertion of sodium-ions into them. Moreover, the presence of oxygen-containing groups increases the number of edge and vacancy defects in the carbon skeleton, thereby enhancing the actual capacity of the material. Studies have indicated that different pre-oxidation times have varying impacts on the electrochemical properties of hard carbon materials. This study used discarded moso bamboo as the raw material, and the optimal pre-oxidation duration of bamboo-based hard carbon was determined to be 4.5 h through a series of comparative experiments. A high-performance biomass-derived hard carbon material was prepared via a stepwise sintering process. It exhibited a specific capacity of 301.4 mAh·g^{-1} at 0.1 C and a first-cycle Coulombic efficiency of 87%.

Keywords: sodium-ion battery; hard carbon anode; moso bamboo; pre-oxidize; performance

Academic Editor: Je Moon Yun

Received: 8 January 2025
Revised: 24 January 2025
Accepted: 25 January 2025
Published: 1 February 2025

Citation: Chen, Y.; Cui, J.; Wang, S.; Xu, W.; Guo, R. Biomass-Derived Hard Carbon Materials for High-Performance Sodium-Ion Battery. *Coatings* **2025**, *15*, 156. https://doi.org/10.3390/coatings15020156

1. Introduction

The advent of social science and technology has given rise to an increased demand for large-scale energy storage devices. The promotion of green energy has led to a growing emphasis on electrochemical energy storage technology. In recent years, the rapid development of new energy vehicles and electronic equipment has brought about a substantial increase in lithium-ion battery production [1]. However, limited lithium resources pose a significant challenge to the long-term development of China's energy storage industry. Therefore, it is essential to explore alternative energy storage technologies to replace lithium-ion batteries.

Sodium metal and lithium have analogous physicochemical properties, reaction potentials, and reaction mechanisms in sodium-ion batteries (SIBs) and lithium-ion batteries [2]. Moreover, sodium resources are abundant and cost-effective, and sodium-ion batteries can potentially replace lithium-ion batteries on a large scale [3]. Sodium metal shares similar properties with lithium; however, the ionic size of the sodium-ion (0.102 nm) is significantly larger than that of the lithium-ion (0.076 nm), which presents substantial challenges in the research and development of anode materials for sodium-ion batteries [4,5]. Since

commercial graphite has a layer spacing of 0.34 nm, it encounters difficulties regarding sodium-ion intercalation and the lack of graphite intercalation compounds (GICs) in the battery, thus impeding its application as an anode material for sodium-ion batteries [6,7]. The development of high-performance anode materials featuring low voltage, high capacity, and stable cycling is crucial to the progress of sodium-ion batteries.

Current research on sodium storage anode materials mainly focuses on carbon-based materials, alloy materials, and so on [8]. Manickam Minakshi et al. [9] synthesized nickel molybdate ($NiMoO_4$) anode materials for sodium-ion batteries using the solution combustion method. They investigated the influence of oxidant concentration on the structure, morphology, and electrochemical properties of the materials. Their findings provided a reference for the optimization of anode materials for sodium-ion batteries. Niyaz Ahmad et al. [10] prepared porous carbon using dense melon rind as a raw material. They investigated the performance of supercapacitors by comparing the effects of different pretreatment methods on the melon peel feedstock and incorporating a novel gel polymer electrolyte (GPE). Their results provided a reference for applying biomass waste to the energy storage field. Manickam Minakshi et al. [11] converted mango seed husks into activated carbon for supercapacitors through carbonization and chemical activation methods. They investigated the influence of activation temperature on material performance. Their findings provided a reference for the resourceful utilization of biomass waste and the development of high-performance carbon materials. Mouad Dahbi [12] prepared hard carbon materials for sodium-ion batteries with a capacity of 333 $mAh{\cdot}g^{-1}$ and a first-cycle Coulombic efficiency of 83.9% using argan nut shells as a raw material. The effects of carbonization temperature, acid treatment, and binder on the structure and electrochemical properties of hard carbon were investigated. Uldana Kydyrbayeva et al. [13] prepared a hard carbon anode material from buckwheat seeds. They carried out a pre-oxidation treatment on the seeds followed by pyrolysis at a specific temperature. The prepared material exhibited a capacity of 327.82 $mAh{\cdot}g^{-1}$ and a first-cycle Coulombic efficiency of 46.29%. Li et al. [14] prepared pre-oxidized asphalt-based hard carbon (OPHC) via a pre-oxidation and high-temperature carbonization process. The OPHC material had a capacity of 333.7 $mAh{\cdot}g^{-1}$ and a first-cycle Coulomb efficiency of 50.97%.

In this research, hard carbon materials were fabricated from waste moso bamboo, serving as biomass feedstock, via a multi-step temperature sintering technique. The unpreoxidized precursor was sintered at a series of stepwise temperatures. As a result, it achieved a specific capacity of 274 $mAh{\cdot}g^{-1}$ at 0.1 C. This process led to a first-cycle Coulombic efficiency as high as 80.9% and a capacity retention of 68.7%. Oxygen-containing functional groups were introduced by employing H_2O_2 as a pre-oxidizing agent, which augmented the defect degree and sodium storage active sites within the graphite flakes. By optimizing the pre-oxidation duration to 4.5 h, a hard carbon material with a capacity of 301.4 $mAh{\cdot}g^{-1}$ at 0.1 C was obtained, along with an elevation in the initial Coulombic efficiency to 87% and a capacity retention rate of 86.2%. In this study, high-performance hard carbon anode materials were prepared using cost-effective biomass feedstock, namely moso bamboo, combined with a multi-step temperature sintering process. In terms of commercializing sodium-ion batteries, this process presents a preferable option for anode materials.

2. Experiment

2.1. Laboratory Reagents and Equipment

In this experiment, the ZYHM-200S ball mill (produced by Beyond Electronic Technology (Shanghai) Co., Ltd., Shanghai, China) was used for ball milling. The KSL-1400X-A2 muffle furnace (produced by Hefei Kexing Material Technology Co., Ltd., Hefei, China) was

used for high-temperature sintering, and 30% hydrogen peroxide (AR grade, provided by Xilon Chemical Reagent Co., Ltd., Shantou, China) was used for pre-oxidation experiments.

2.2. Materials Preparation and Synthesis

A total of 500 g of waste moso bamboo material was collected. Its surface was cleaned and dried in an oven at 80 °C for 24 h. After drying, the moso bamboo material was crushed, and the resulting crushed product was sieved using a 360-mesh screen. Subsequently, 100 g of the sieved powder was weighed and placed in a tube furnace. It was heated to 225 °C at a heating rate of 3 °C/min in an N_2 atmosphere and held at this temperature for 2 h (first temperature step). The carbonized material obtained in the first stage was sieved using a 150-mesh screen. The sieved carbonized material was then heated to 500 °C at a heating rate of 3 °C/min in an N_2 atmosphere and held at this temperature for 3 h (second temperature stage). At the end of the second stage, 30% hydrogen peroxide with a solid/liquid ratio of 1:8 was added to the carbonized material, and the mixture was soaked for different durations ranging from 45 min to 6 h. The soaked carbonized material was ball-milled for 1 h. Subsequently, it was heated to 1350 °C at a heating rate of 3 °C/min in an N_2 atmosphere and held at this temperature for 3 h. This third temperature step was carried out to obtain bamboo-based hard carbon powder. The samples with different pre-oxidation duration were labeled as B1 (unsoaked), B2 (soaked for 45 min), B3 (soaked for 1.5 h), B4 (soaked for 3 h), B5 (soaked for 4.5 h), and B6 (soaked for 6 h), respectively.

2.3. Sample Characterization

Scanning electron microscopy (SEM, model S5000, manufactured by Shanghai Caikang Optical Instrument Co., Shanghai, China) was employed to observe the microstructure. Additionally, D/max-rB type X-ray powder diffraction was used to carry out a structural analysis of the crystals. Surface defects were analyzed using inVia micro-Raman spectroscopy. Energy-dispersive spectroscopy (EDS, model S5000, manufactured by Shanghai Caikang Optical Instrument Co., Shanghai, China) was used to analyse the composition of hard carbon elements.

2.4. Battery Assembly and Electrochemical Performance Testing

The sodium-ion storage performance of the sample hard carbon was evaluated by assembling 2032 coin cells. The active materials, conductive carbon black, and poly(vinylidene fluoride) were dissolved in an appropriate amount of N-methyl-2-pyrrolidone at a mass ratio of 8:1:1. The mixture was stirred for 5 h to form a homogeneous slurry, which was then coated onto copper foils and dried in a vacuum oven at 80 °C for 12 h. Each electrode contained 2 $mg \cdot cm^{-2}$ of active materials. Sodium metal sheets were employed as counter electrodes, and glass fiber separators (model 1827-047,Whatman, Maidstone, UK) were used. The electrolyte composition consisted of 1.0 M $NaPF_6$ dissolved in a 1:1 volumetric mixture of ethylene carbonate (EC) and diethyl carbonate (DEC). Cyclic voltammetry (CV) measurements were carried out using a Metrohm electrochemical workstation (model PAR273A, manufactured by Princeton Applied Research, Oak Ridge, TN, USA) with an initial voltage range of 0.01–3.00 V and a scan rate of 0.1 $mV \cdot s^{-1}$. A NEWARE BTS-5 V20 mA device was used for battery charge/discharge testing. The above electrochemical measurements were performed at ambient temperatures (25 °C–30 °C).

3. Results and Discussion

As illustrated in Figure 1, scanning electron microscope (SEM) images of the six samples reveal that samples B1, B2, B3, B4, and B5 exhibit a characteristic hard carbon structure, characterized by the presence of small lumps with irregular shapes and uneven sizes [15]. As the pre-oxidation time increases, the pores in samples B1 to B5 become larger

and more numerous. The presence of these larger pores has been proven to enhance the material's capacity for both adsorption and ion transport [16].

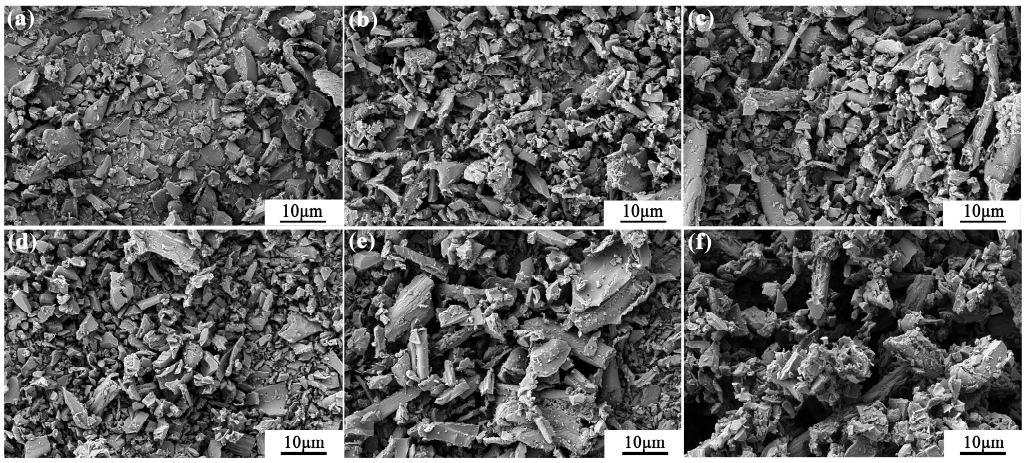

Figure 1. The SEM images of (**a**) B1, (**b**) B2, (**c**) B3, (**d**) B4, (**e**) B5, and (**f**) B6.

As depicted in Figure 2, the elemental mapping of the six samples shows a uniform distribution of carbon and oxygen elements within the material. Figure 2f illustrates the elemental distribution when the pre-oxidation time is set to 6 h. In this case, the C element is uniformly dispersed, while the O element is concentrated in areas with increased porosity and defects, thereby forming a local oxygen-rich region [17].

Table 1 presents the C and O elemental mass fractions of the six samples. As shown in Table 1, the C elemental mass fraction decreases while the O elemental mass fraction increases with the extension of the pre-oxidation time. This trend is attributed to the adsorption and decomposition of H_2O_2 by the hard carbon precursor during the pre-oxidation process. As a result, the oxygen-containing groups enter the carbon layer, and the oxygen content rises [18].

Table 1. Sample C, O element mass fraction, and surface area table.

Type	C (wt%)	O (wt%)	S_{BET} (m^2/g)
B1	97.93	2.07	3.8
B2	97.63	2.37	3.9
B3	97.40	2.60	4.1
B4	96.66	3.34	4.6
B5	96.29	3.71	4.9
B6	96.23	3.77	5.0

Figure 3 presents the XRD diffraction patterns, Raman diffraction patterns, and trends of the six samples. As depicted in Figure 3a, the XRD diffraction patterns of B1, B2, B3, B4, B5, and B6 all exhibited characteristic diffraction peaks of hard carbon near 24° and 44°, corresponding to the (002) crystalline facet and the (100) crystalline facet, respectively [19,20]. The (002) characteristic peak indicates that the hard carbon material is a typical amorphous material with a low degree of graphitization and irregular layer spacing. As the pre-oxidation time increases, the diffraction angle of the (002) crystal plane gradually decreases while the layer spacing increases. The large layer spacing facilitates the embedding and transport of sodium-ions [21]. Additionally, the microporous nature of hard carbon affords an 'elastic space' for sodium-ion storage, thereby reducing the stress caused by volume expansion to a certain extent. The characteristic peak of (100) is caused by SP^2 hybridization, suggesting that the graphite microcrystals of hard carbon are disordered

and small in size [22]. The interlayer distance d was calculated for six groups of samples using the Bragg equation with:

$$n\lambda = 2d\sin\theta \quad (1)$$

n denotes the order of diffraction; λ represents the wavelength of the incident X-rays; θ represents half of the angle of incidence or half of the diffraction angle; d is commonly used to denote the interplanar spacing of the crystal.

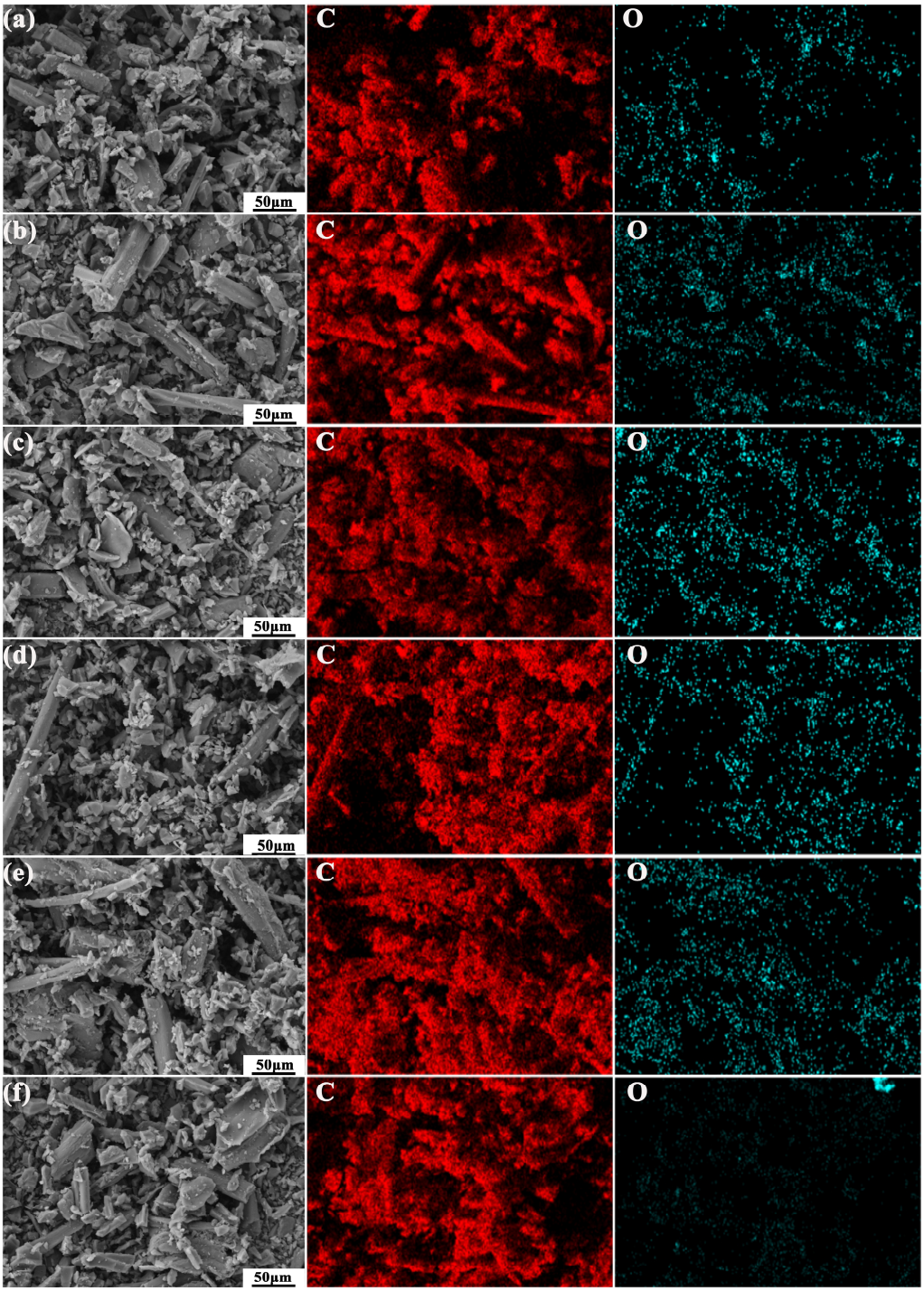

Figure 2. The EDS elemental mapping of images (**a**) B1, (**b**) B2, (**c**) B3, (**d**) B4, (**e**) B5, and (**f**) B6.

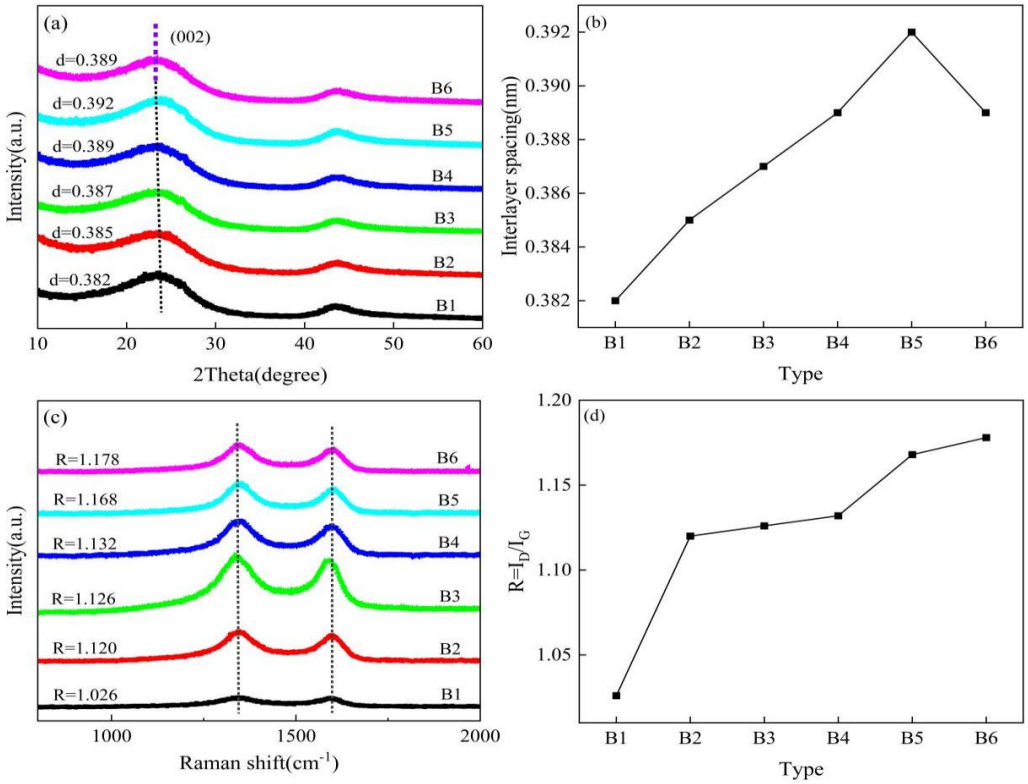

Figure 3. (**a**) XRD diffraction pattern of hard carbon B1, B2, B3, B4, B5, B6; (**b**) trend plot of carbon layer spacing of hard carbon B1, B2, B3, B4, B5, B6; (**c**) Raman diffraction pattern of hard carbon B1, B2, B3, B4, B5, B6; (**d**) R = ID/IG of hard carbon B1, B2, B3, B4, B5, B6 trend plot.

The calculations based on Equation (1) provide the following results: d(B1) = 0.382 nm, d(B2) = 0.385 nm, d(B3) = 0.387 nm, d(B4) = 0.389 nm, d(B5) = 0.392 nm, and d(B6) = 0.389 nm. As shown in Figure 3b, the XRD data of samples B1, B2, B3, B4, B5, and B6 display a distinct trend. As depicted in Figure 3b, the layer spacing of hard carbon first increases and then decreases with the increase in pre-oxidation time. A long pre-oxidation time leads to the disordered expansion of pores and the collapse of holes within the material. Consequently, the loose carbon layer structure is rearranged into a compact one [23–25]. The Raman diffraction patterns of the six samples are presented in Figure 3c. As shown in Figure 3c, the six samples display two distinctive characteristic peaks typical of hard carbon materials, namely 1360 cm^{-1} (D peak) and 1600 cm^{-1} (G peak) [26]. The D peak characterizes defects like vacancies and edges in the material, while the G peak reflects the orderliness of the graphite structure. The G peak is commonly used to characterize the material's orderliness. Here, I_D represents the intensity value of the D peak in the Raman test, and I_G represents the intensity value of the G peak in the Raman test. Moreover, the value of R (where $R = I_D/I_G$) is negatively correlated with the degree of orderliness [27]. The G-peak is ascribed to the sp^2 hybridized carbon in the material, which undergoes ordered intraplane stretching vibration. The D-peak, on the other hand, is related to defects such as grain boundaries, vacancies, and disordered structures. In highly ordered materials, the sp^2 hybridized carbon is arranged orderly, leading to a high G-peak intensity, a low D-peak intensity, and a small I_D/I_G value. Conversely, materials with a high defect density show an increase in D-peak intensity, a decrease in G-peak intensity, and a rise in the I_D/I_G value. Consequently, the I_D/I_G value of hard carbon materials is inversely proportional to their degree of order [28,29]. Through a rigorous calculation process, the following R values were obtained: R(B1) = 1.026, R(B2) = 1.120, R(B3) = 1.126, R(B4) = 1.132, R(B5) = 1.168, and R(B6) = 1.178. As depicted in Figure 3d, there is a clear trend in the R

value. Figure 3d shows a positive correlation due to a large number of oxygen-containing functional groups, which leads to an increase in edge and vacancy defects and a rise in structural disorder [30]. The presence of edge and vacancy defects in hard carbon has been shown to enhance the number of active sites available for sodium-ion adsorption. As a result, sodium-ion distribution becomes more uniform, which helps disperse stress generated during sodium-ion intercalation, reducing local stress concentration.

Figure 4a presents the first charge–discharge curves of the six samples at a current density of 30 $mA \cdot g^{-1}$. As depicted in the figure, the initial Coulombic efficiencies of B1, B2, B3, B4, B5, and B6 are 80.9%, 28.1%, 80.7%, 85.5%, 87.0%, and 72.0%, respectively. Sample B5 shows the highest first Coulomb efficiency and a relatively symmetric charge/discharge profile, indicating favorable reversibility of sodium-ions in B5. Conversely, B2 has an initial Coulombic efficiency of merely 28.1% and a marked difference in the charge/discharge curves, demonstrating poor reversibility of sodium-ions in B2. As demonstrated in Figure 4b, the charge–voltage change curves of the six samples under consideration disclose a notable aspect of B1's redox peak curve. Although it exhibits a smooth profile, it lacks complete symmetry. This observation indicates the presence of stable sodium-ion transport, along with a certain amount of irreversible capacity [31]. The existence of stray peaks in the reduction peak of B2 highlights a crucial point: insufficient pre-oxidation time is due to the poor quality of the solid electrolyte interlayer (SEI) formed on the hard carbon surface, the inadequate optimization of the pore structure, and the increased sodium-ion resistance during the initial insertion, which impedes effective storage and diffusion [32,33]. As depicted in B3 and B4 of Figure 4b, the poor symmetry of the redox peaks and the presence of spurious peaks in the oxidation peaks suggest that the pre-oxidation generated a significant number of defective sites. In turn, these defective sites induced additional side reactions during the oxidation reaction, leading to spurious peaks. It has been demonstrated that the enhancement of surface activity after oxidation treatment can facilitate the rapid adsorption and incorporation of sodium-ions, enhancing the reduction reaction kinetics. As a result, the reduction peaks in B3 and B4 show increased sharpness [34,35]. As depicted in B5 of Figure 4b, the redox peaks display heterogeneity and are relatively sharp, a characteristic that indicates the presence of more defects within the hard carbon. Among the six samples, the redox peak of B5 is the most prominent, implying that B5 has many sodium-ion adsorption sites with strong adsorption performance and can accommodate a significant amount of sodium-ions [36]. As depicted in B6 of Figure 4b, the redox peak curve features a smooth profile and clearly defined peaks, signifying that the structural ordering of B6 is enhanced. This enhancement can be ascribed to the extended oxidation process, which leads to disordered pore expansion, pore collapse, and carbon layer rearrangement. A comprehensive characterization of the peaks in the DQ/DV curves reveals that B5 possesses a favorable crystal structure and pore structure, which provide smoother diffusion channels and more stable reaction sites for sodium-ions. This enables sodium-ions to undergo charge/discharge reactions in a more reversible manner. By contrast, the poor structure of B2 impedes the diffusion and reaction of sodium-ions, leading to a decrease in reversibility. Moreover, it was found that the hard carbon achieved the highest first Coulombic efficiency when the pre-oxidation time was 4.5 h.

Figure 5 presents the analyzed capacity curves for the six samples, data plots for 100 cycles at a current density of 60 $mA \cdot g^{-1}$, and rate performance plots at various current densities. As depicted in Figure 5a, the specific capacities of the six samples were 274 $mAh \cdot g^{-1}$, 95.2 $mAh \cdot g^{-1}$, 289.3 $mAh \cdot g^{-1}$, 311.4 $mAh \cdot g^{-1}$, 301.4 $mAh \cdot g^{-1}$, and 244.4 $mAh \cdot g^{-1}$, respectively. The significant decrease in B2 capacity is attributed to two reasons. Firstly, the incomplete oxidation reaction and the scarcity of oxygen-containing groups led to the

hard carbon's poor surface activity, which restricted the intercalation of sodium-ions and resulted in a capacity decrease. Secondly, although oxidation can modify the microstructure of the hard carbon, the pores were not optimized for the efficient storage of sodium-ions due to the short oxidation time [37,38]. The slope capacity of the pre-oxidized hard carbon material increases significantly while the platform capacity decreases. This is primarily because of the strong oxidation of H_2O_2, which generates a large number of edge defects. During the charging and discharging process, sodium-ions are preferentially adsorbed by these sites, contributing to the increase in slope capacity [39,40]. B5's plateau capacity is considerably higher than B3, B4, and B6. On the one hand, the appropriate pre-oxidation time inhibits the overgrowth of graphite microcrystals, and a large number of closed pores are formed, providing sufficient space for the insertion and storage of sodium-ions and thereby enhancing the plateau capacity [41]. On the other hand, a reasonable oxidation time can effectively regulate the pore structure, facilitating the sodium-ions to enter the interior of the material and further improving the plateau capacity [42,43].

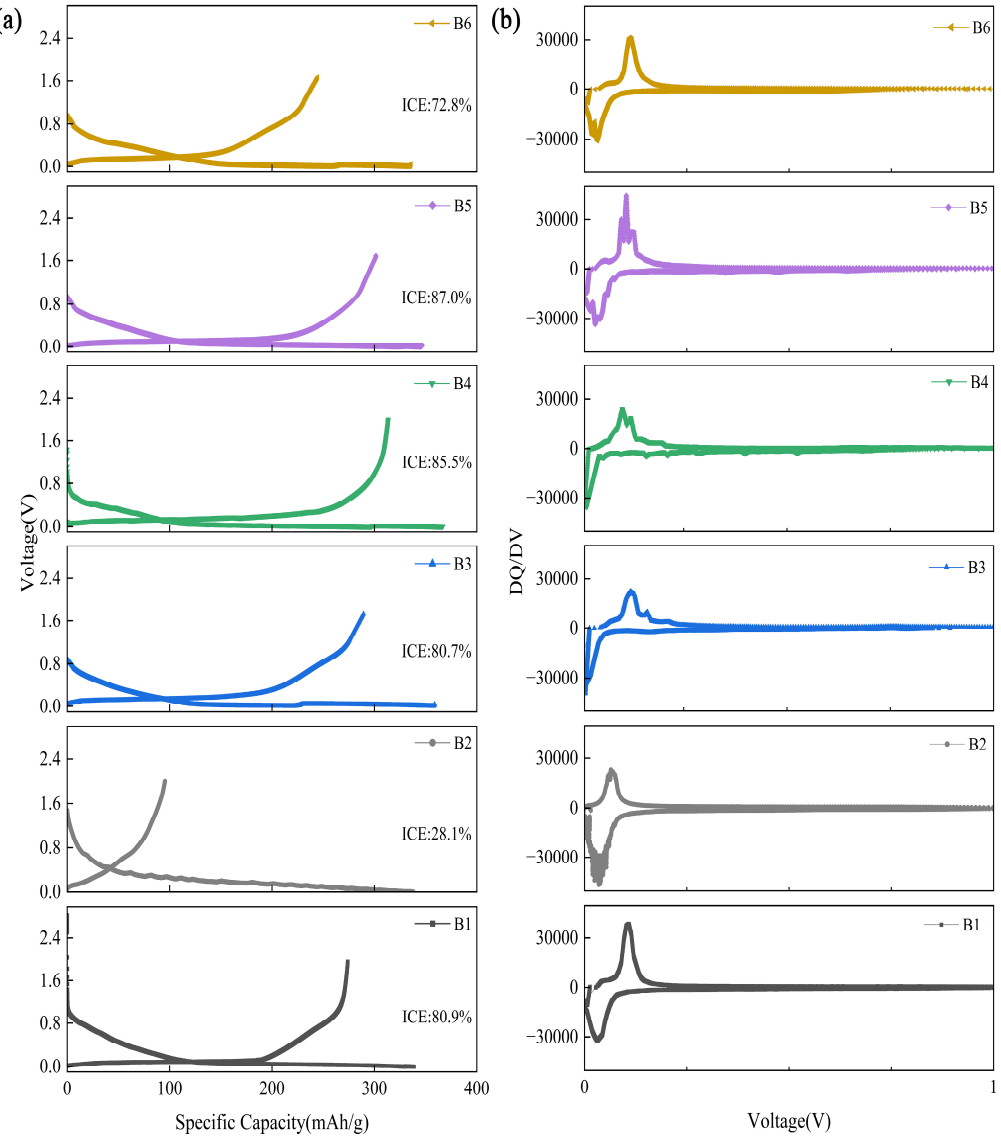

Figure 4. (**a**) First charge–discharge curves of hard carbon B1, B2, B3, B4, B5, B6, at 30 mA·g^{-1}; (**b**) Charge–voltage variation (DQ/DV) curves of hard carbon B1, B2, B3, B4, B5, B6.

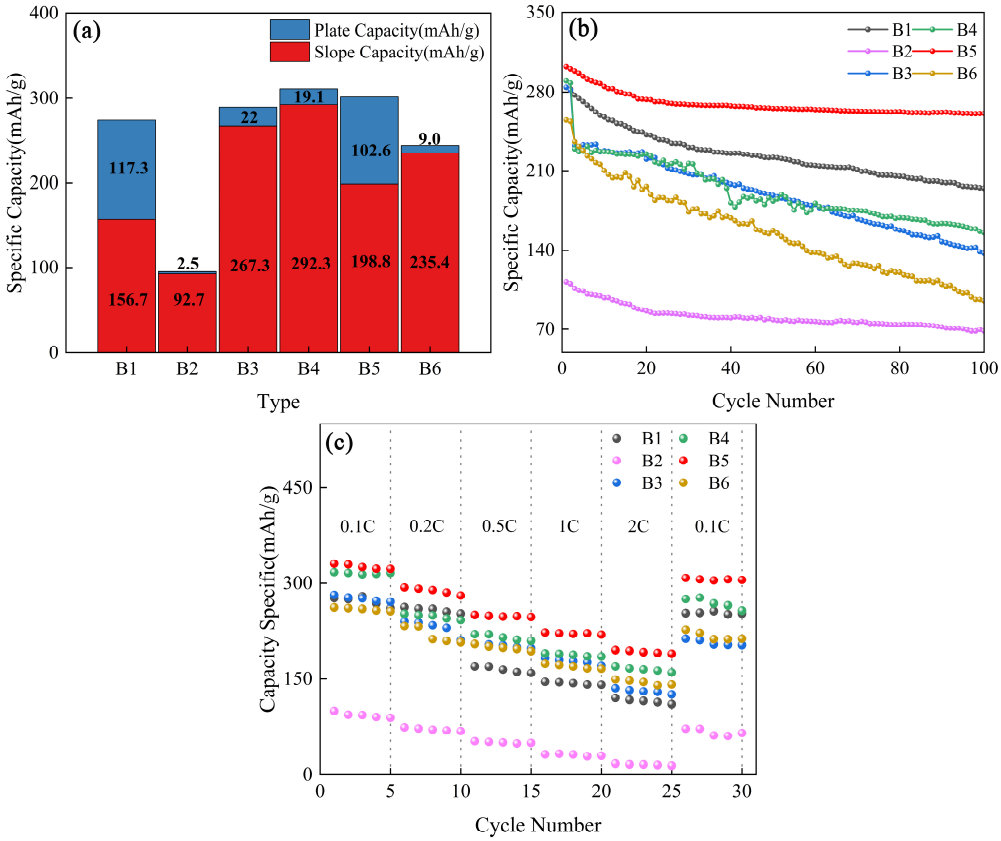

Figure 5. (**a**) Volume analysis plots for hard carbon samples B1, B2, B3, B4, B5, and B6; (**b**) cycle stability of hard carbon samples B1, B2, B3, B4, B5, and B6 at a current density of 60 mA·g^{-1}; (**c**) rate performance of hard carbon samples B1, B2, B3, B4, B5, and B6.

As depicted in Figure 5b, the capacity retention rates of B1, B2, B3, B4, B5, and B6 during 100 cycles were 68.7%, 61.0%, 48.3%, 53.3%, 86.2%, and 38.0%, respectively. The capacities of B1, B2, B3, B4, and B6 decreased continuously throughout the first 100 cycles, suggesting that the batteries had poor cycling stability. By contrast, B5 did not exhibit any significant increase or decrease during 100 cycles, indicating that B5 possesses excellent cycle stability. As depicted in Figure 5c, sample B5 demonstrated good electrochemical performance under different current densities. Specifically, it provides a reversible specific capacity of 195.9 mAh·g^{-1} at a high discharge multiplier of 2 C. B1 only had a reversible specific capacity of 120.2 mAh·g^{-1} at a magnification of 2 C. Moreover, the cell was found to have excellent cycling stability. Among the six samples, B5 has the best plateau capacity, slope capacity, and cycling stability, demonstrating that 4.5 h of pre-oxidation is the optimal time for the preparation of hard carbon using moso bamboo as a precursor.

4. Conclusions

The use of waste moso bamboo as the main raw material, along with a multi-step temperature sintering process and pre-oxidation treatment, was adopted to introduce oxygen-containing groups into the hard carbon layer. This method was carried out to increase the carbon layer spacing, thus improving the initial Coulombic efficiency and capacity of the cell. The optimal pre-oxidation time was explored through a combination of scanning electron microscopy (SEM), energy-dispersive spectroscopy (EDS), X-ray diffraction (XRD), Raman spectroscopy, and electrochemical characterization. Eventually, after the completion of the second-stage carbonization, a pre-oxidation time of 4.5 h was found to result in a high-performance biomass-derived hard carbon material with a specific capacity of 301.4 mAh·g^{-1}, an initial Coulombic efficiency of 87%, and excellent cycling stability at

a current density of 30 $mAh \cdot g^{-1}$. The current paper proposes a novel strategy to improve the sodium storage performance of hard carbon materials.

Author Contributions: Conceptualization, Y.C.; Formal analysis, W.X.; Resources, S.W.; Data curation, R.G.; Writing—original draft, Y.C.; Supervision, S.W.; Project administration, J.C. All authors have read and agreed to the published version of the manuscript.

Funding: Funding was provided by Lanzhou University of Technology (Grant No. 2022CYZC-20).

Institutional Review Board Statement: Not applicable.

Informed Consent Statement: Not applicable.

Data Availability Statement: Data is contained within the article.

Conflicts of Interest: The authors declare that they have no known competing financial interests or personal relationships that could have influenced the work reported in this paper.

References

1. Shao, W.; Shi, H.; Jian, X.; Wu, Z.-S.; Hu, F. Hard-carbon anodes for sodium-ion batteries: Recent status and challenging perspectives. *Adv. Energy Sustain. Res.* **2022**, *3*, 2200009. [CrossRef]
2. Zhang, F.; Yao, Y.; Wan, J.; Henderson, D.; Zhang, X.; Hu, L. High temperature carbonized grass as a high performance sodium ion battery anode. *ACS Appl. Mater. Interfaces* **2017**, *9*, 391397. [CrossRef] [PubMed]
3. Cao, J.M.; Zhang, K.Y.; Yang, J.L.; Gu, Z.Y.; Wu, X.L. Differential bonding behaviors of sodium/potassium-ion storage in sawdust waste carbon derivatives. *Chin. Chem. Lett.* **2024**, *35*, 109304. [CrossRef]
4. Chen, X.; Liu, C.; Fang, Y.; Ai, X.; Zhong, F.; Yang, H.; Cao, Y. Understanding of the sodium storage mechanism in hard carbon anoeds. *Carbon Energy* **2022**, *4*, 10031284. [CrossRef]
5. Chen, Y.; Sun, H.; He, X.; Chen, Q.; Zhao, J.; Wei, Y.; Wu, X.; Zhang, Z.; Jiang, Y.; Chou, S. Pre-oxidation strategy transforming waste foam to hard carbon anodes for boosting sodium storage performance. *Small* **2023**, *20*, 2307132. [CrossRef] [PubMed]
6. Xiao, B.; Rojo, T.; Li, X. Hard carbon as sodium-ion battery anodes progress and challenges. *ChemSusChem* **2019**, *12*, 133144. [CrossRef]
7. Deng, W.; Cao, Y.; Yuan, G.; Liu, G.; Zhang, X.; Xia, Y. Realizing improved sodium-ion storage by introducing carbonyl groups and closed micropores into a biomass derived hard carbon anode. *ACS Appl. Mater. Interfaces* **2021**, *13*, 4772847739. [CrossRef]
8. Ying, H.J.; Han, W.Q. Metallic Sn-Based Anode Materials: Application in High-Performance Lithium-Ion and Sodium-Ion Batteries. *Adv. Sci.* **2017**, *11*, 1700298. [CrossRef]
9. Minakshi, M.; Barmi, M.; Mitchell, D.R.; Barlow, A.J.; Fichtner, M. Effect of oxidizer in the synthesis of $NiMoO_4$ anchored nanostructure nickel molybdate for sodium-ion battery. *Mater. Today Energy* **2018**, *10*, 114.
10. Ahmad, N.; Rinaldi, A.; Sidoli, M.; Magnani, G.; Vezzoni, V.; Scaravonati, S.; Pontiroli, D. Pre-treated biomass waste melon peels for high energy density semi solid-state supercapacitors. *J. Power Sources* **2024**, *624*, 235511. [CrossRef]
11. Wickramaarachchi, W.A.M.K.P.; Minakshi, M.; Gao, X.; Dabare, R.; Wong, K.W. Hierarchical porous carbon from mango seed husk for electro chemical energy storage. *Chem. Eng. J. Adv.* **2021**, *8*, 100158. [CrossRef]
12. Lei, X.; Zhang, L.; Guo, X.; Tian, Q.; Fan, X.; Tong, H.; Yang, Y. Regulation of composition, microstructure, and pore structure of biomass-based hard carbon to boost the sodium storage performance. *J. Energy Storage* **2024**, *101*, 113792. [CrossRef]
13. Yan, B.; Han, C.; Dai, Y.; Li, M.; Wu, Z.; Gao, X. Biomass derived hard carbon materials for sodium ion battery anodes: Exploring the influence of carbon source on structure and sodium storage performance. *Fuel* **2024**, *371*, 132141. [CrossRef]
14. Dahbi, M.; Kiso, M.; Kubota, K.; Horiba, T.; Chafik, T.; Hida, K.; Matsuyama, T.; Komaba, S. Synthesis of Hard Carbons from Argan Shell for Na-Ion Batteries. *J. Mater. Chem. A* **2017**, *5*, 99179928. [CrossRef]
15. Kydyrbayeva, U.; Baltash, Y.; Mukhan, O.; Nurpeissova, A.; Kim, S.S.; Bakenov, Z.; Mukanova, A. The buckwheat-derived hard carbon as an anode material for sodium-ion energy storage system. *J. Energy Storage* **2024**, *96*, 112629. [CrossRef]
16. Cao, B.; Li, X.F. Recent Progress on Carbon-based Anode Materials for Na-ion Batteries. *Acta Phys.-Chim. Sin.* **2020**, *36*, 1905003.
17. Wang, H.; Niu, H.; Shu, K.; Sun, L.; Wang, Y.; Du, Y.; Kang, Y.M. Regulating the "core-shell" microstructure of hard carbon through sodium hydroxide activation for achieving high-capacity SIBs anode. *J. Mater. Sci. Technol.* **2025**, *209*, 161170. [CrossRef]
18. Slater, M.D.; Kim, D.; Lee, E.; Johnson, C.S. Sodium-Ion Batteries. *Adv. Funct. Mater.* **2013**, *23*, 32553255. [CrossRef]
19. Xie, F.; Xu, Z.; Guo, Z.; Titirici, M.-M. Hard carbons for sodium ion batteries and beyond. *Prog. Energy* **2020**, *2*, 042002. [CrossRef]
20. Li, Y.; Lu, Y.; Meng, Q.; Jensen, A.C.S.; Zhang, Q.; Zhang, Q.; Tong, Y.; Qi, Y.; Gu, L.; Titirici, M.; et al. Regulating pore structure of hierarchical porous waste cork derived hard carbon anode for enhanced Na storage performance. *Adv. Energy Mater.* **2019**, *9*, 1902852. [CrossRef]

21. Li, Y.; Yang, Y.; Lin, R.; Zhang, C.; Xiao, T.; Ma, Z.; Ma, X. Enhancing electrochemical performance in sodium ion batteries: Strategic modification of oxygen-containing functional groups in hard carbon. *Fuel* **2025**, *381*, 133397. [CrossRef]
22. Stevens, D.A.; Dahn, J.R. The Mechanisms of Lithium and Sodium Insertion in Carbon Materials. *J. Electrochem. Soc.* **2001**, *148*, A803A811. [CrossRef]
23. Fang, C.; Huang, Y.; Zhang, W.; Han, J.; Deng, Z.; Cao, Y.; Yang, H. Routes to High Energy Cathodes of Sodium-Ion Batteries. *Adv. Energy Mater.* **2016**, *6*, 1501727. [CrossRef]
24. Ni, Q.; Bai, Y.; Wu, F.; Wu, C. Polyanion-Type Electrode Materials for Sodium-Ion Batteries. *Adv. Sci.* **2017**, *4*, 1600275. [CrossRef]
25. Chu, Y.; Zhang, J.; Zhang, Y.; Li, Q.; Jia, Y.; Dong, X.; Xiao, J.; Tao, Y.; Yang, Q. Reconfiguring hard carbons with emerging sodium ion batteries: A perspective. *Adv. Mater.* **2023**, *35*, 2212186. [CrossRef]
26. Wang, Z.; Yang, H.; Liu, Y.; Bai, Y.; Chen, G.; Li, Y.; Lu, J. Analysis of the Stable Interphase Responsible for the Excellent Electrochemical Performance of Graphite Electrodes in Sodium-Ion Batteries. *Small* **2020**, *16*, 2003268. [CrossRef]
27. Sun, F.; Wang, H.; Qu, Z.; Wang, K.; Wang, L.; Gao, J.; Lu, Y. Carboxyl dominant oxygen rich carbon for improved sodium ion storage: Synergistic enhancement of adsorption and intercalation mechanisms. *Adv. Energy Mater.* **2021**, *11*, 2002981. [CrossRef]
28. Arie, A.A.; Tekin, B.; Demir, E.; Demir-Cakan, R. Hard carbons derived from waste tea bag powder as anodes for sodium ion battery. *Mater. Technol.* **2019**, *34*, 515524. [CrossRef]
29. El Moctar, I.; Ni, Q.; Bai, Y.; Wu, F.; Wu, C. Hard Carbon Anode Materials for Sodium-Ion Batteries. *World Sci.* **2018**, *11*, 1830003. [CrossRef]
30. Zhao, Y.; Ye, J.; Zhang, P.; Li, Z.; Zhao, H. Abnormal preferential oxygen functionalization on the surface of soft/hard carbon for sodium storage. *Appl. Surf. Sci.* **2022**, *602*, 154336. [CrossRef]
31. Lou, Z.; Wang, H.; Wu, D.; Sun, F.; Gao, J.; Lai, X.; Zhao, G. Microcrystalline regulation of bituminous coal derived hard carbon by pre-oxidation strategy for improved sodium-ion storage. *Fuel* **2022**, *310*, 122072. [CrossRef]
32. Qian, J.; Chen, Y.; Wu, L.; Cao, Y.; Ai, X.; Yang, H. High capacity Na-storage and superior cyclability of nanocomposite Sb/C anode for Na-ion batteries. *Chem. Commun.* **2012**, *48*, 70707072. [CrossRef] [PubMed]
33. Xiao, L.; Lu, H.; Fang, Y.; Sushko, M.L.; Cao, Y.; Ai, X.; Yang, H.; Liu, J. Low-defect and low-porosity hard carbon with high coulombic efficiency and high capacity for practical sodium ion battery anode. *Adv. Energy Mater.* **2018**, *8*, 1703238. [CrossRef]
34. Wang, Y.; Feng, Z.; Zhu, W.; Gariépy, V.; Gagnon, C.; Provencher, M.; Laul, D.; Veillette, R.; Trudeau, M.L.; Guerfi, A.; et al. High capacity and high efficiency maple tree-biomass-derived hard carbon as an anode material for sodium ion batteries. *Materials* **2018**, *11*, 1294. [CrossRef]
35. Chen, X.; Tian, J.; Li, P.; Fang, Y.; Fang, Y.; Liang, X.; Cao, Y. An overall understanding of sodium storage behaviors in hard carbons by an "adsorption-intercalation/filling" hybrid mechanism. *Adv. Energy Mater.* **2022**, *12*, 2200886. [CrossRef]
36. Li, Y.; Qian, J.; Zhang, M.; Wang, S.; Wang, Z.; Li, M.; Bai, Y.; An, Q.; Xu, H.; Wu, F.; et al. Co-Construction of Sulfur Vacancies and Heterojunctions in Tungsten Disulfide to Induce Fast Electronic/Ionic Diffusion Kinetics for Sodium-Ion Batteries. *Adv. Mater.* **2020**, *32*, 2005802. [CrossRef]
37. Simone, V.; Boulineau, A.; de Geyer, A.; Rouchon, D.; Simonin, L.; Martinet, S. Hard carbon derived from cellulose as anode for sodium ion batteries: Dependence of electrochemical properties on structure. *J. Energy Chem.* **2016**, *25*, 761768. [CrossRef]
38. Zhao, L.F.; Hu, Z.; Lai, W.H.; Tao, Y.; Peng, J.; Miao, Z.C.; Dou, S.X. Hard carbon anodes: Fundamental understanding and commercial perspectives for Na-ion batteries beyond Li-ion and K-ion counterparts. *Adv. Energy Mater.* **2021**, *11*, 2002704. [CrossRef]
39. Sun, D.; Zhao, L.; Sun, P.; Zhao, K.; Sun, Y.; Zhang, Q.; Ma, X. Rationally Regulating Closed Pore Structures by Pitch Coating to Boost Sodium Storage Performance of Hard Carbon in Low-voltage Platforms. *Adv. Funct. Mater.* **2024**, *34*, 2403642. [CrossRef]
40. Ma, R.; Chen, Y.; Li, Q.; Zhang, B.; Chen, F.; Leng, C.; Jia, D.; Guo, N.; Wang, L. Oxygen-driven closing pore formation in coal-based hard carbon for low-voltage rapid sodium storage. *Chem. Eng. J.* **2024**, *493*, 153389. [CrossRef]
41. Xu, T.; Qiu, X.; Zhang, X.; Xia, Y. Regulation of surface oxygen functional groups and pore structure of bamboo-derived hard carbon for enhanced sodium storage performance. *Chem. Eng. J.* **2023**, *452*, 139514. [CrossRef]
42. Wahid, M.; Puthusseri, D.; Gawli, Y.; Sharma, N.; Ogale, S. Hard carbons for sodium ion battery anodes: Synthetic strategies, material properties, and storage mechanisms. *ChemSusChem* **2018**, *11*, 506526. [CrossRef] [PubMed]
43. Zhang, G.; Zhang, L.; Ren, Q.; Yan, L.; Zhang, F.; Lv, W.; Shi, Z. Tailoring a Phenolic Resin Precursor by Facile Pre-oxidation Tactics to Realize a High-Initial-Coulombic-Efficiency Hard Carbon Anode for Sodium-Ion Batteries. *ACS Appl. Mater. Interfaces* **2021**, *13*, 3165031659. [CrossRef] [PubMed]